Report for course "Soil* deformation: Measurements, Modelling, Visualization"

Anders Damsgaard Christensen

adc@cs.au.dk, http://cs.au.dk/~adc

Last revision: November 8, 2011

Contents

1 Introduction

This report is the final assignment for the course "Soil Deformation: Modelling, Measurements, and Visualization", held at Research Centre Foulum September 26th to October 1st, 2011. The course homepage is:

`https://djfextranet.agrsci.dk/sites/deformation/public/Pages/front.aspx`

The report is divided into four parts, corresponding to the overall subjects of the course. Each part is based on a self-chosen assignment, and is independent. Since my background is in glacial geology, I will try to highlight any specific interest in the subjects, and formulate and test hypotheses of direct relation to the field.

With regards to formatting, bold notation in mathematical formulas denotes vectors, and dots denote time-derivatives. References to external litterature are found at the end of the paper.

*Soil is sexy

2 Lab measurements

2.1 Precompression stress

In theory, the soil deformation during e.g. compression takes place in an initial, reversible, elastic phase, before shifting to irreversible plastic deformation at higher strains. When determining the precompression stress, the prior maximal value of stress is found by applying stress until the plastic phase is reached.

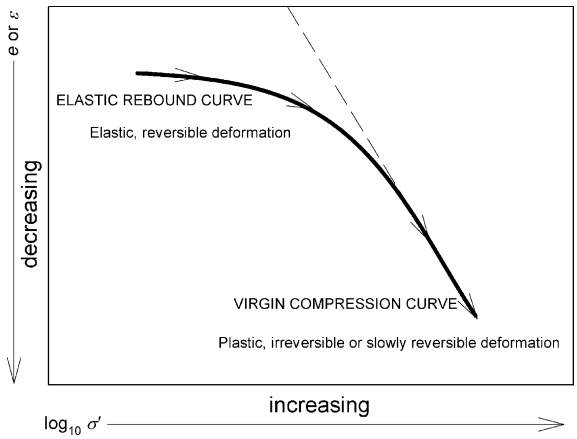

Figure 1: Idealized stress-strain relationship during soil compression. The strain is represented as either vertical strain (ϵ) or the void ratio (e). From Gregory et al. (2006).

The stress-strain relationship is visualized by plotting log the logarithmic stress values, e.g. $\log(p)$, against volumetric strain, ϵ_p. There are a number of possible stress paths in this system according to the material rheology. The virgin compression line is the straight line that is followed when a (new) maximum value of stress is applied, where the compression index is the slope of the virgin compression line. The recompression line is the straight line that the material follows in the plot when stress is reapplied, but at lower streses than the previous maximal stresses. The recompression lines are assumed to be parallel, and the recompression index is the slope of the recompression line. The precompression stress has in glaciology been used to determine the palaeo-subglacial stresses excerted to the sediment. The effective subglacial stress is decomposed into porewater pressure (p_w) and the ice overburden weight (σ_0). The effective stress (σ') is the ice overburden weight with the porewater pressure subtracted. Field measurements (Bartholomaus et al., 2011, e.g.) show that the subglacial porewater pressure is highly dynamic in response to seasonal and diurnal fluctuations in ablation and changes in the glacial hydrological system. If we assume that the maximal effective stress corresponds to the *lowest* porewater pressure during the relative thickest ice cover, we can estimate the ice sheet thickness.

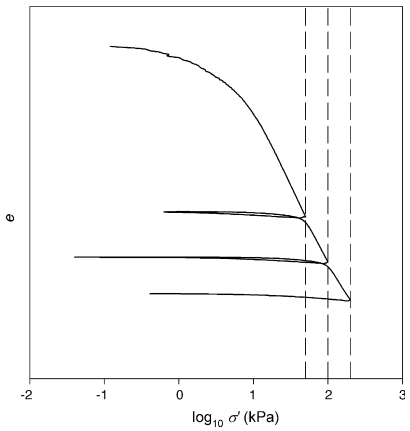

Figure 2: Stress strain path during repeated loading/unloading. Note that the recompression lines are not completely straight and parallel, however close to it. From Gregory et al. (2006).

The past ice advances from the Scandinavian Ice Sheet have had decreasing lateral extent and vertical thickness, and glacial depositions have been correlated to specific ice sheet advances by looking at the differences in precompressional stress values.

2.2 Macromechanical properties

The macromechanical properties angle of internal friction (ϕ) and cohesion (C) are defined as the linear representation of the value of the material shear strength (τ^*) under a range of effective normal pressures (σ'). The Mohr-Coulomb criterion describes the upper limit for shear stress acting along slip planes in an *ideal Coulomb material*:

$$|\tau| \leq C + \sigma' \tan \phi \tag{1}$$

The parameters can be constrained from laboratory tests in e.g. a shearing device, where annular shearing- or ring-shearing (torsional) apparatuses

minimize the end-zone effects associated with direct shear boxes. The used apparatus will usually measure the applied effective stress, the shear stress (or the torque in rotational shearing) and the dilation. Figure 3 shows an idealistic version of sensor readings when shearing a granular material. The shearing can be subdivided into four stages (Li and Aydin, 2010):

1. At the beginning, the shearing results in contraction, caused by elastic deformation of the grains and further reorganization of the particle assemblage towards smaller volume (Taylor, 1948) in the new, stronger stress field (the stress is now a product of the perpendicular shear stress τ and effective stress σ'.

2. The assemblage dilates due to beginning particle movement Reynolds (1885). At the end of this period, the peak shear strength will be reached (τ_u).

3. The shear strength of the material decreases unto a steady state. The shear zone evolves into a high-porosity layer, with a minimal thickness of 5–10 grain diameters in non-cohesive granular material (de Gennes, 1999). The grain activation intensity decays exponentially with the distance from the center of the shear band (Herrmann, 2001).

4. In the final, *critical* state, the shear will display no low-frequency volumetric changes, only high-frequency fluctuations caused by the granularity of the material, and the reorganization of the force-bearing system within (Li and Aydin, 2010).

If the material is not preconsolidated, the the shear stress and dilation will increase to the critical state without passing through a maximum (Nedderman, 1992).

The macromechanical properties can be further divided into apparent (peak) values, ϕ_a and C_a, and effective values, ϕ' and C'. The apparent (peak) values are determined as the maximum value measured during shear, denoted as τ_u. The effective values are derived from the critical state shear strength of the material. In saturated granular materials, the effective strength has the value of the normal stress with the porewater pressure subtracted; $\sigma' = \sigma_0 - p_\mathrm{w}$.

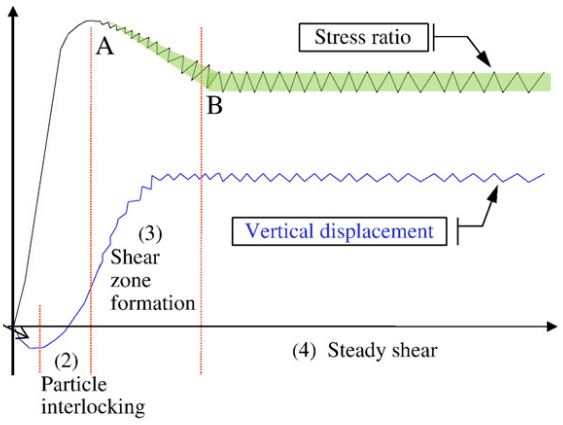

Figure 3: A four-stage shearing model for preconsolidated granular materials in direct shear. From Li and Aydin (2010).

The shear experiment is repeated on preferably new material, otherwise homogenized material, under a different effective stress. The peak- and effective shear stress values are recorded along with applied normal stress values. Figure 4 shows an example of a linear regression to constrain macromechanical properties of a number of shear experiments.

2.3 Air permeability during progressive strain

The air permeability is a direct measurement of the porespace network, and is a function of the size of the pore spaces and the degree of interconnection of the voids. It can be measured during compression or shear by recording the air flow rate required to maintain a steady value of the pressure gradient between two opposite sample boundaries.

The airflow is assumed to be laminar, and an integrated form of Darcy's law is calculated with:

$$Q = \frac{k_a \Delta p a_s}{\eta L_s} \tag{2}$$

where Q is the measured volumetric flow rate, Δp is the pressure difference, a_s is the cross-sectional area, k_a is the air permeability, and L_s is the height of the sample. The air viscosity is $\eta_\mathrm{air} = 1.827 \times 10^{-5}\,\mathrm{kg\,m^{-1}\,s^{-1}}$.

During compression, interaggregate pores are less stable than cylindrical macropores, and pores

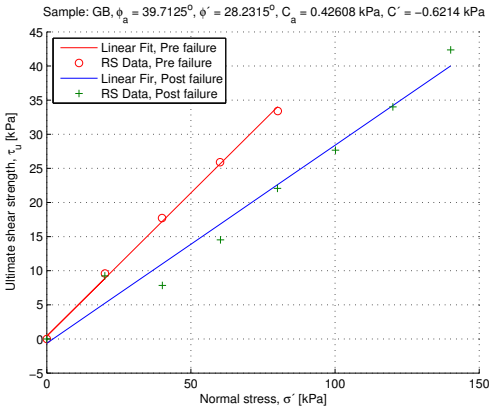

Figure 4: $(\sigma', \tau_\mathrm{u})$- and (σ', τ')-plot and linear regression of ring-shear data, performed on a well-sorted granular material. Constrained macromechanical properties are $\phi_\mathrm{a} = 39.7°$ and $C_\mathrm{a} = -0.4\,\mathrm{kPa}$ and $\phi' = 28.2°$ and $C' = -0.6\,\mathrm{kPa}$. It should be noted that the true cohesion cannot be negative and thus should be assumed to be zero.

parallel to the maximal stress field gradient are mechanically more stable than oblique pores (Schaffer et al., 2008).

The dynamics of the porespace ratio is very interesting in the context of progressive shear strain, as they have a high potential impact on the mechanical properties of shear zones in saturated materials with low hydraulic conductivity. During deformation of a saturated granular material, the void ratio will increase during plastic deformation (Reynolds, 1885), which leads to a decrease in the porewater pressure in the shear zone. As the effective pressure is increased (recall that $\sigma' = \sigma_0 - p_w$), the Mohr Coulomb criterion predicts an increase of the shear strength (Iverson, 2010). If the relationship between the shear velocity and the hydraulic conductivity is sufficiently high, the hydraulic gradient will not have sufficient time to reestablish pressure equilibrium. The net effect is a *strain hardening*. The shear zone would thus tend to relocate to a weaker part. If the shear is driven not by constant shear velocity, but constant shear stress, the resulting shear displacement will be periodic, discrete events (Iverson, 2010).

These considerations however treat grain crushing as neglectible, and it should be kept in mind that it can have a high potential effect onto the grain size distribution in the shear zone, demonstrated in e.g. Sassa et al. (2004). The grain crushing will reduce the volume/thickness of the shear zone, resulting in an opposite increase in the porewater pressure, i.e. a possible *strain softening*. For this reason, it is necessary to consider the mechanical durability of the shear zone grains with regard to the magnitude of the force chains in the grain stress network.

3 Pseudoanalytical model

The pseudoanalytical model presented in the following, is used for investigating static problems of stress and strain in soil mechanics. Boussinesq's problem deals with a point load on the surface of an elastic half space (Boussinesq, 1885; Johnson, 1985), where it is possible to calculate the theoretical stress at any point in the half space. If the stress is integrated over a lateral infinite plane parallel to the surface, placed at a certain depth, the value will always equal the point load, independent of the depth. The stress is however more widely spatially distributed with great depth.

3.1 Söhne's summation procedure

SoilFlex is a pseudoanalytical model, in the way that it uses Söhne's summation procedure (se below) to superposition a number of results from the analytical Boussinesq' equation to determine the stress state in an elastic half space, when the upper boundary is stressed by an irregular load area discretized into a number of point loads. Söhne's summation procedure consists of the following:

- The contact area of a non-point load is divided into a number of point loads.
- It is solved by applying the analytical solution for each of these points.
- The model correctly reproduces impacts of load and contact stress

3.2 SoilFlex usage

SoilFlex is an interactive Excel algorithm, backed by Visual Basic macros, aimed at agricultural applications where compaction of the substratum by agricultural vehicles is of interest. The work flow is divided into three steps:

1. Formulation of the upper boundary condition: Stress field normal to the tyre-soil interface. FRIDA model predicts the tyre stress in (x, y)-space based on values for the tyre air pressure, the tyre size, the wheel load and the soil properties. The load can be applied in increments.
2. Söhne's summation procedure in the soil based on the analytical Boussinesq equation (1885): The contact plane is divided into point loads, where each is treated as a Boussinesq problem.
3. The soil strain response to the stress (stress-strain relationship) is chosen from:
   - Gupta and Larson (1982)
   - Bailey and Johnson (1989)
   - O'Sullivan and Robertson (1996)

In relation to field measurements, the stresses are usually underestimated in the top soil, and overestimated in the lower parts. The reason for this can be that the upper model boundary condition is inaccurate, the model for stress propagation is insufficient, or that the soil stress measurements done in the field are inaccurate.

SoilFlex has capabilities of handling vertical strain in two ways; 1) Uniaxial inferred strain, where the vertical strain equals the volumetric strain constrained from e.g. triaxial tests, and 2) plane strain, where the vertical strain is a function of both the volumetric strain and the shear strain. Plane strain is closer to the real conditions, but needs additional input parameters which are often not available.

3.3 Stress-strain models

In the following, the variations in the predicted bulk density between two different stress-strain models is investigated.

Two identical single wheels with wheel load 3000 kg, a tyre inflation pressure of 724 kPa, a tyre width of 0.50 m, and a diameter of 1.13 m are simulated. The resulting contact area and pressure is shown in figure 5. The mesh resolution is 0.05 m.

The surface-parallel shear stress are neglected, and only the vertical stresses are calculated (σ_z). Figure 6 shows the vertical stress with depth along the $(x = 0, y = 0, z)$ line.

The substratum is chosen to consist of a single soil layer with a thickness of 1.50 m. The soil cohesion is set to $C = 60$ kPa and the angle of internal friction is $\phi = 20°$. These and the soil mechanical properties were held constant between the different stress-strain models.

The input data to the O'Sullivan and Robertson (1996) stress strain model is based on precompressional compaction parameters, where the slope of

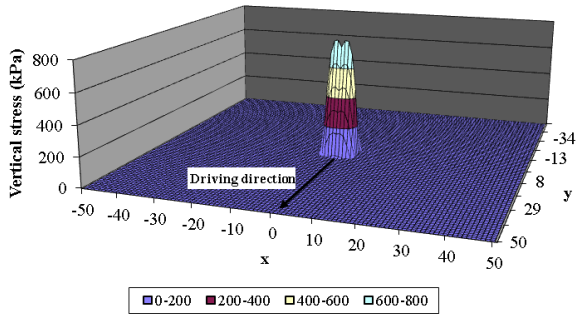

Figure 5: Contact area of wheel and theoretical load, calculated by SoilFlex.

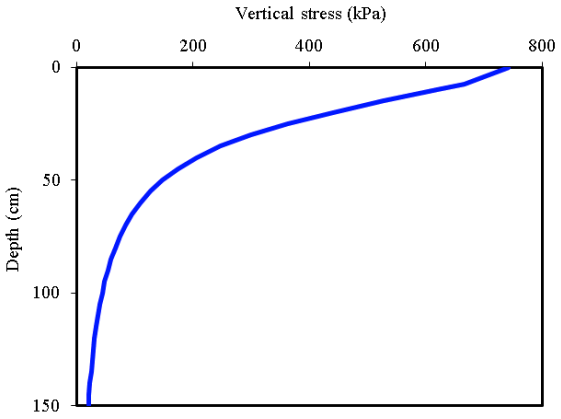

Figure 6: Vertical stress with depth, calculated by SoilFlex.

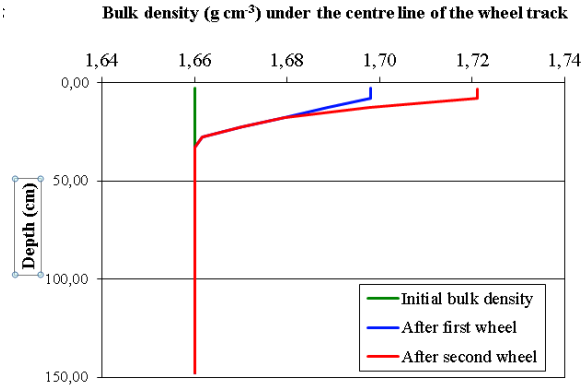

Figure 7: Compaction model by O'Sullivan and Robertson (1996).

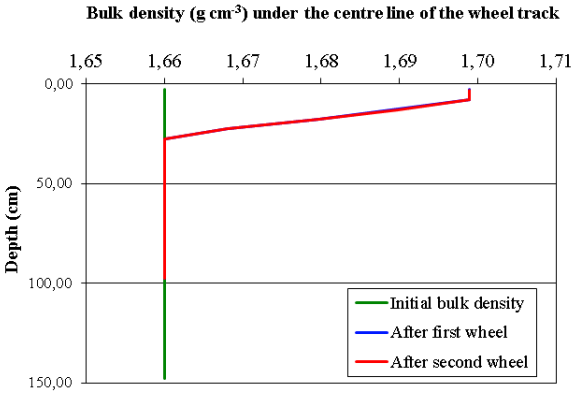

Figure 8: Compaction model by Gupta and Larson (1982).

the virgin compressional line and the recompressional line among other parameters are set. Se figure 7 for variations of the bulk density with depth. This model predicts an initial increase in the density in the uppermost 0.3 m of the soil. After the second wheel has passed, the density is increased even further. This implies that this model predicts plastic deformation, even when the second load is identical to the first one.

The Gupta and Larson (1982) model is adjusted by setting parameters based of the the virgin compression line, parameters related to the saturation of the soil, and others. Figure 8 shows the predicted strain from this model. A major difference is that the application of the second, identical, wheel load does not result in further plastic deformation, which fits to precompression theory.

The O'Sullivan and Robertson (1996) predicts a higher bulk density of the uppermost soil. The depth of the plastic deformation is close to identical between the two models.

4 Finite Element Modelling

Finite Element Modelling (FEM) is a numerical technique for finding approximate solutions for partial differential equations (PDEs). FEM is a good technique fpr describing any physical phenomena of continuum bodies (soil, liquid, gas) that can be captured mathematically with a PDE, e.g. deformation of a solid body due to applied stress or fluid and heat flow through porous materials.

Most PDEs cannot be solved analytically because the boundary conditions are too complicated, the material properties are heterogeneous and/or anisotropic, the constitutive laws are non-linear or the processes that the PDEs describe are coupled.

The basic concept is that a body or structure may be discretized into smaller elements of finite dimensions and homogeneous properties called finite elements. The original body or structure is then considered as an assemblage of finite elements as nodes in the finite element mesh. Equilibrium equations at each element ensure continuity at each node. The temporal domain is also discretized to observe non-steady state systems.

4.1 Problem description

Glacial water transport can take place in a variety of ways (figure 9). The majority of the meltwater is transported subglacially, either in a *distributed* mode, where it flows as groundwater flow in the subglacial bed or in a thin film at the ice-bed interface, and/or in a *non-distributed* (discrete) mode through channels. These channels can be carved up into the ice (Röhtlisberger), typically when the ice is resting on stable bedrock surfaces. On soft, deformable beds, the non-distributed flow takes place in Nye-channels (or N-channels) instead, that are eroded into the sedimentary bed. On the upper boundary of the channel, the cryogenic pressure of the slow-flowing ice will try to make the ice move into the channel, while the meltwater pressure and/or -heat keeps the channel open. Meanwhile the meltwater erodes into the subglacial bed, and the deformable bed can creep into the channel from below. In these situations, the bed will tend to be softer than the glacial ice.

I will use a FEM model to simulate the situation where the meltwater flow in the channel has ceased, and the relative soft bed creeps into the channel.

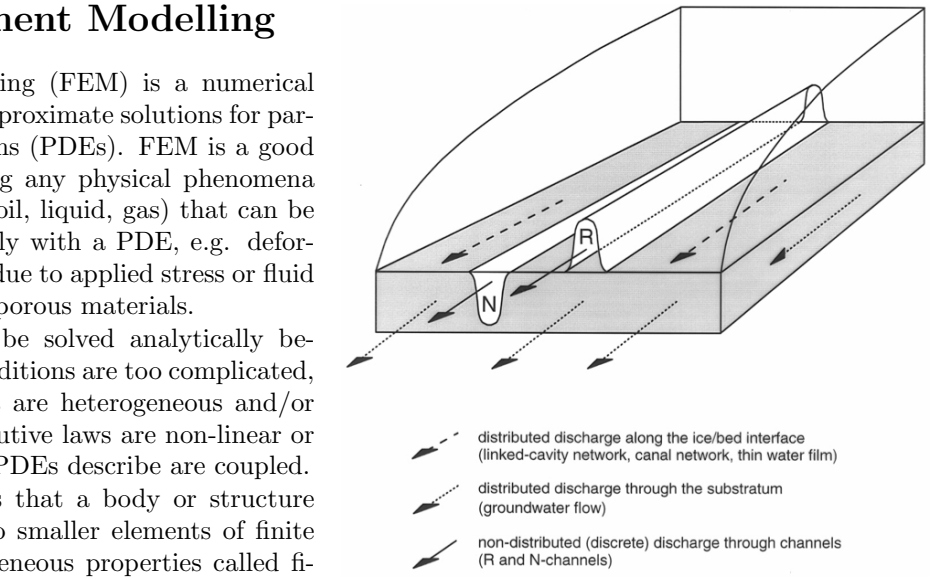

Figure 9: Types of glacial water transport. Subglacial bed: grey, glacier: transparent, arrows: flow paths

The model geometry is displayed in figure 10.

4.2 COMSOL setup

COMSOL Multiphysics is used for model setup, numerical computation and data analysis. The problem is formulated as a 2D "Structural Mechanics (solid)" setup. The study type is time dependent to allow continuous deformation of the sediment.

The right and left boundaries (10) are given the "roller" boundary condition (no friction). The upper left and upper right boundaries (marked with red color) are excerting a prescribed stress downwards of 85 kPa, a value in the range of effective normal pressures beneath glaciers and ice sheets (Cuffey and Paterson, 2010). The channel boundaries are free to move. The mesh is physics-controlled (automatically generated) with an extra fine element size, resulting in 5442 elements. The grid is configured for adaptive mesh refinement, so areas with the highest numerical gradients recive finer mesh nodes after automatical remeshings during the computations. The model is run from time 0 s to 10 s with output every 0.1 s.

The sedimentary bed is given the behavior close to a subglacial till. Young's modulus was $E = 207 \times 10^6$ Pa, Poisson's ratio was $\nu = 0.3$, the den-

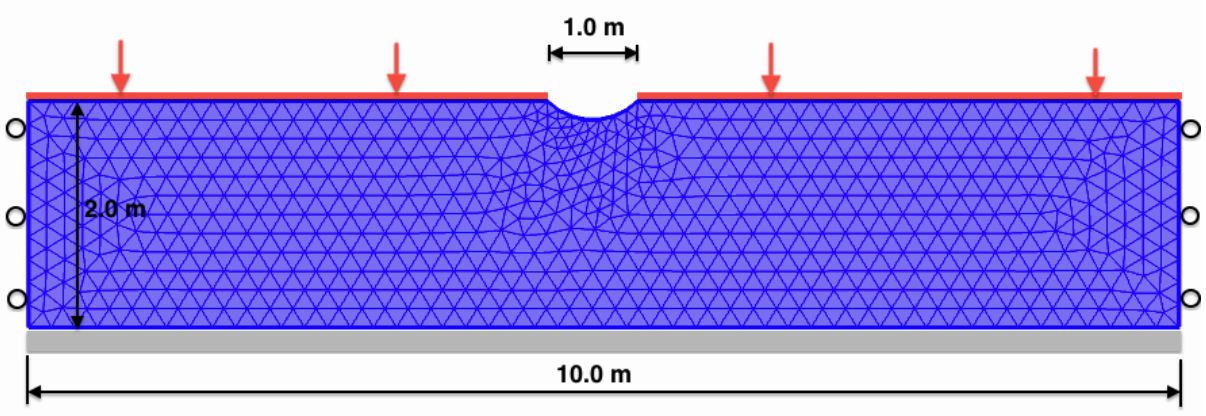

Figure 10: Model geometry and initial, automatic mesh. The channel is 0.20 m deep.

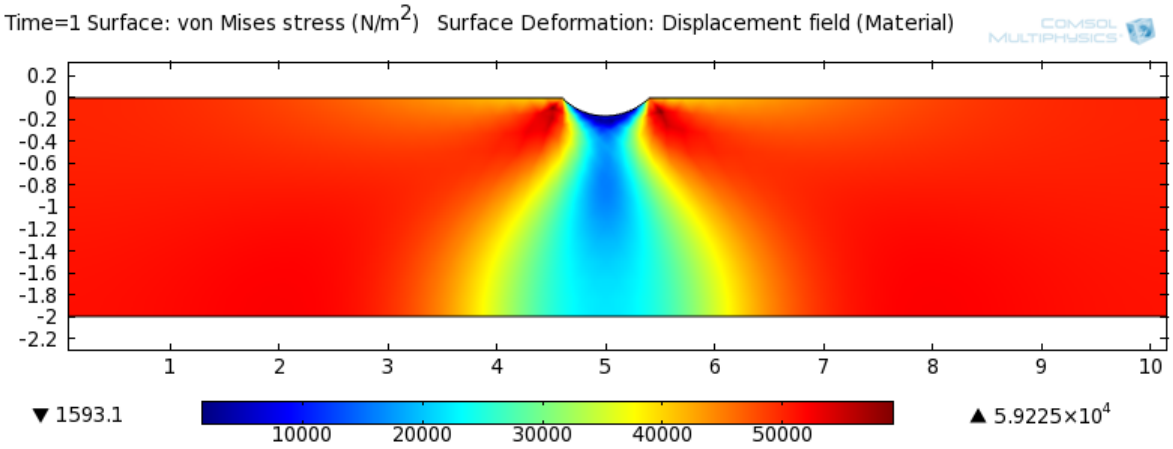

Figure 11: Soil stress magnitude at time $t = 10.0\,\mathrm{s}$.

sity was $\rho = 1700\,\mathrm{kg\,m^{-1}}$, the angle of internal friction was $\phi = 17°$, and the cohesion was $C = 60\,\mathrm{kPa}$. The bed was set to deform with the COMSOL "Soil Plasticity" model, and given the Mohr-Coulomb yield criterion.

4.3 Results

Figure 11 shows the magnitude of the stress in the sediment at the end of the simulation. When increasing the surface scale factor, it becomes apparent that the sediment has started to creep into the void. The magnitude of this creep is however notably low. Therefore this mechanism seems unlikely to cause the channel closure.

The sediment close to the channel floor is exerted with a very low effective pressure (blue colors in figure 11). The sediment would be in a loose state, since the Mohr-Coulomb criteria based shear strength is proportional to the effective pressure. This implies that it would be very easy for the meltwater to erode the channel floor as soon as the channel meltwater pressure drops beneath the value of the cryogenic ice pressure. This suggests how ceasing meltwater channels could act as effective erosional agents of the substratum, which is a very interesting result and to my knowledge not yet considered within glacial geology. The erosive effect of subglacial channels is documented in the geomorphological tunnel-valley structures, where the mode of erosion has been widely discussed (Jørgensen and Sandersen, 2006).

5 Discrete Element Modelling

The Discrete Element Method (DEM, also called the distinct element method) (Cundall and Strack, 1979) simulates the physical behavior and interaction of discontinuous material, and is ideal for simulating the dynamic behavior of granular material. In this exercise, a capillary bond approximation was incorporated in a three-dimensional model, and the macroscopic behavior and stability was evaluated.

5.1 Theory

In this DEM formulation, each particle is a discrete, unbreakable unit with its own mass and inertia, and the assemblage dynamics are examined under the influence of e.g. gravity and boundary conditions such as moving walls. In this case, the particles are treated as spherical entities, which reduces the complexity of contact search and -dynamics. Based on the net forces applied, the movement and rotation of each particle is calculated during each small time step (Δt) by application of Newton's law of motion for entities with constant mass:

$$m\ddot{\mathbf{x}} = \mathbf{F} \qquad I\dot{\omega} = \mathbf{T} \tag{3}$$

where m is the particle mass, $\mathbf{x}$ is the particle position vector and $\mathbf{F}$ is the total force vector. I is the moment of inertia, ω is the angular velocity and $\mathbf{T}$ is the total rotational moment. A second-order scheme based on the Taylor expansion was chosen as the integration scheme on the base of accuracy and simplicity (Kruggel-Emden et al., 2008).

Using the *soft body contact model*, the time is discritized into small steps (typically $\Delta t \approx 10^{-8}$), and the particles are allowed to overlap (overlap denoted δ). For a particle pair a and b:

$$\delta_{ab} = ||\mathbf{x}_a - \mathbf{x}_b|| - (r_a + r_b) \tag{4}$$

where r represents the individual particle radius. If $\delta < 0$, there is an overlap of the particles. The normal vector between the two particles is calculated from the vector between the particle centers:

$$\mathbf{n}_{ab} = \frac{\mathbf{x}_{ab}}{||\mathbf{x}_{ab}||} \tag{5}$$

From the overlap, a contact model is used to constrain the normal- and tangential components of the resulting repulsive force, in this case modelled with a linear-elastic model, where the tangential shear force is limited by the Mohr-Coulomb constitutive model. The linear-elastic model was chosen over Hertzian models due to the results of Di Renzo and Di Maio (2004), which reported a better fit to experimental data with linear formulations. The spring constant at the contact normal is given a reduced value for the unloading of the contact than during the loading, to simulate energy dissipation by plastic deformation caused by the contact (Walton and Braun, 1986):

$$\mathbf{f}_n = -k^n_{ab}\delta_{ab}\mathbf{n}_{ab} \quad \text{(loading)} \tag{6}$$

$$\mathbf{f}_n = -k^n_{ab}\alpha\delta_{ab}\mathbf{n}_{ab} \quad \text{(unloading)} \tag{7}$$

where k^n_{ab} is the elastic stiffness of the contact (a global value of $k^n = 10^5\,\mathrm{N\,m^{-1}}$ was used), $\mathbf{n}_{ab}$ is the normal vector between the particle position vectors, and $\alpha \in]0;1]$ is a dimensionless constant for incorporating the dissipative energy loss (a value of $\alpha = 0.9$ was used). The tangential shear force component is a nonlinear relation limited by friction (Richefeu et al., 2006, e.g.):

$$\mathbf{f}_s = -\min(\gamma_t||\dot{\delta}^t||, \mu||\mathbf{f}_n - \mathbf{f}_c||)\frac{\dot{\delta}^t}{||\dot{\delta}^t||} \tag{8}$$

where γ_t denotes the tangential viscosity of the contact. The shear velocity vector is calculated as:

$$\dot{\delta}^t_{ab} = \dot{\mathbf{x}}_{ab} - (\dot{\mathbf{x}}_{ab} \cdot \mathbf{n}_{ab})\mathbf{n}_{ab} \tag{9}$$

The liquid bond force $\mathbf{f}_c$ were introduced using the simple capillary bond implementation proposed by Richefeu et al. (2006), which is simple to implement while still providing realistic results. The capillary attraction is implemented as a force law expressing the capillary force as a function of the distance, water volume, and particle diameters (see Richefeu et al. (2006) for details on the algorithm).

It is based on an exponential decay of the contractive cohesional capillary force below the debonding distance (δ^{debond}). θ is the surface wettability, V_b is the liquid bond volume, R is the geometrical mean of the two particle radii, and λ is a non-static value accounting for the exponential decay of the bond strength with distance. The values were set to $\theta = 0$ and $V_b = 1 \times 10^{-12}\,\mathrm{m^3}$, and the tangential viscosity was given a value of $\gamma_t = 1\,\mathrm{N\,s\,m^{-1}}$.

$$\kappa = 2\pi\gamma_t \cos\theta \tag{10}$$

$$\delta^{\text{debond}} = \left(1 + \frac{\theta}{2}\right) V_b^{1/3} \tag{11}$$

$$f_n^c = \begin{cases} -\kappa R & \delta_{ab} \leq 0 \\ -\kappa R e^{\delta_{ab}/\lambda} & 0 \leq \delta_{ab} \leq \delta^{\text{debond}} \\ 0 & \delta^{\text{debond}} < \delta_{ab} \end{cases} \tag{12}$$

This approach assumes that there is sufficient liquid for all possible bonds, and that the bond is instantaneously formed when the particles are within the debonding distance. The algorithm could possibly be improved by having seperate bonding- and debonding distances, where the bonding distance is of smaller length. This approach would however also require management of the contact history, and is thus less parallel in nature.

5.2 Implementation

This three-dimensional DEM algorithm is formulated for GPU computation using the C/C++ CUDA API (NVIDIA, 2010a), which takes advantage of the parallel nature of the problem. The shear force component formulation in equation 8 was chosen over incremental shear force formulations to make the contact force calculations even more parallel, and avoiding the need for contact history bookkeeping. Each component of the contact search-, contact model-, and integration computations for each particle is a single-instruction, multiple-data problem, suited for the massively parallel structure of the GPU streaming multiprocessors (Kirk and Hwu, 2010; NVIDIA, 2010b). The neighbor search is reduced by discretizing the spatial model domain into a uniform, cubic grid with Thrust sorted cell lists. The algorithm checks wether the cell size is sufficient to include the debonding distance.

Visualization of the particle assemblage is performed using a custom CUDA ray-tracing algorithm. The capillary bonds were not rendered.

Simple walls are implemented, parallel to the world coordinate system. The wall-sphere collisions are treated as inelastic collisions with a 10% energy loss.

5.3 Results

A number of experiments were conducted with the algorithm, figure 12 shows an example of 5832 particles clustering together due to the cohesive capillary forces. Gravity was disabled to better visualize the clustering in a static image.

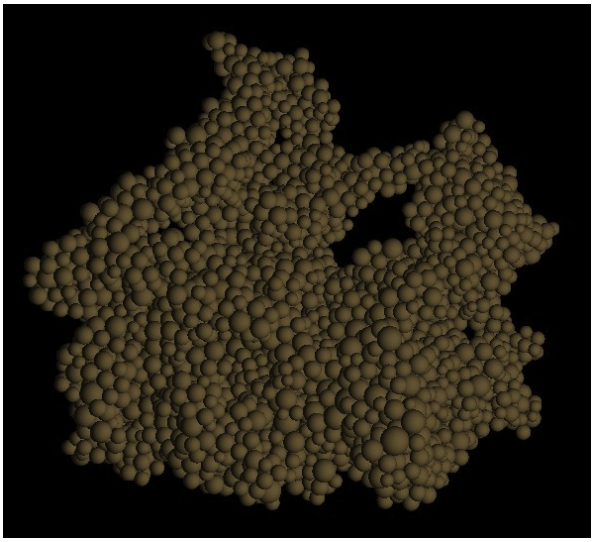

Figure 12: 5832 particles in experiment with capillary bonds. The simulation domain has the dimensions $3 \times 3 \times 3$ cm.

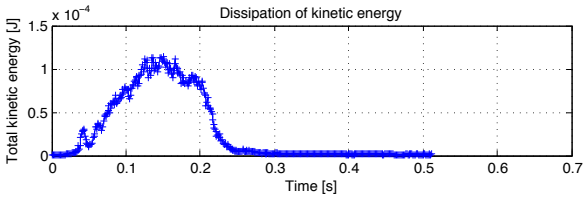

Figure 13: Total kinetic energy.

Figure 13 shows the total kinetic energy of the system at time t by calculating the sum of the kinetic energy of all N particles:

$$E_{\text{kin}} = \sum_{i=1}^{N} \frac{1}{2} \left(\frac{4}{3}\pi r_i^3 \rho_i\right) v_i^2 \tag{13}$$

where ρ is the particle material density (in this case $\rho = 3600\,\text{kg}\,\text{m}^{-3}$), and v is the particle velocity. The plot shows an initial increase in kinetic energy due to capillary cohesion when the general interparticle distance is $0 < \delta < \delta^{\text{debond}}$. The energy starts to dissipate when it is lost in contact collisions (eq. 6, 7 and 8) when $\delta < 0$.

6 Outlook

What could I use from the course?
As I have had it introduced from a constructional point of view, I had a large interest in the new, agriculturally related angle on geotechnical problems. I was pleasantly surprised how much of the material I can directly reuse when considering the subglacial mechanics. Prior to the course, I was unaware of the geotechnical research activities at Foulum. If possible, I am sure that your extensive laboratory facilities and knowledge in the field will come into high value later during my studies.

My main fields of interest during the course were the review of granular material theory and Molecular Dynamics/Discrete Element Method, as these are most directly related to my work, and are difficult to find included in a course. Even though I have been involved in the subjects for some time now, I still learned a lot of new ways of handling specific tasks. With regards to the laboratory work, I am sure I will find good use of the theory with regards to air permeability when I reach the development phase of the fluid-particle coupling in my Discrete Element model. It seems like a good benchmark for the permeability of the material under different stress conditions.

While it was nice to review the main subjects once again during the preparation of this report, I have to admit that I think the requirements for this final assignment were too extensive and time consuming, relative to other 5 ECTS PhD courses I have participated in. I would however not hesitate to recommend this course to other students within my field, if held again at a later point in time.

References

A.C. Bailey and C.E. Johnson. A soil compaction model for cylindrical stress states. *Transactions of the ASAE*, 32(3):822–825, 1989.

T.C. Bartholomaus, R.S. Anderson, and S.P. Anderson. Growth and collapse of the distributed subglacial hydrologic system of kennicott glacier, alaska, usa, and its effects on basal motion. *Journal of Glaciology*, 57(206):985, 2011.

J. Boussinesq. *Application dès potentiels a l'étude de l'équilibre et du mouvement des solides élastiques*. Gauthier-Villars, 1885.

K.M. Cuffey and WSB Paterson. The physics of glaciers. *Elsevier, ed*, 4:693, 2010.

P.A Cundall and O.D.L. Strack. A discrete numerical model for granular assemblies. *Géotechnique*, 29:47–65, 1979.

P.G. de Gennes. Granular matter: a tentative view. *Reviews of modern physics*, 71(2):374–382, 1999.

A. Di Renzo and F.P. Di Maio. Comparison of contact-force models for the simulation of collisions in dem-based granular flow codes. *Chemical engineering science*, 59(3):525–541, 2004.

A.S. Gregory, W.R. Whalley, C.W. Watts, N.R.A. Bird, P.D. Hallett, and A.P. Whitmore. Calculation of the compression index and precompression stress from soil compression test data. *Soil and Tillage Research*, 89(1):45–57, 2006.

S.C. Gupta and W.E. Larson. Modeling soil mechanical behavior during tillage. *ASA Special Publication-American Society of Agronomy (USA)*, 1982.

H.J. Herrmann. Structures in deformed granular packings. *Granular Matter*, 3(1):15–18, 2001.

N.R. Iverson. Shear resistance and continuity of subglacial till: hydrology rules. *Journal of Glaciology*, 56(200):1104, 2010.

K.L. Johnson. *Contact mechanics*. Cambridge Univ Press, 1985.

F. Jørgensen and P.B.E. Sandersen. Buried and open tunnel valleys in Denmark–erosion beneath multiple ice sheets. *Quaternary Science Reviews*, 25(11-12):1339–1363, 2006.

D.B. Kirk and W-M.W. Hwu. *Programming Massively Parallel Processors*. Morgan Kaufmann, Elsevier, 2010.

H. Kruggel-Emden, M. Sturm, S. Wirtz, and V. Scherer. Selection of an appropriate time integration scheme for the discrete element method (dem). *Computers & Chemical Engineering*, 32 (10):2263–2279, 2008.

Y.R. Li and A. Aydin. Behavior of rounded granular materials in direct shear: Mechanisms and quantification of fluctuations. *Engineering Geology*, 115(1-2):96–104, 2010.

R.M. Nedderman. *Statics and kinematics of granular materials*. Cambridge University Press, Cambridge, 1992.

NVIDIA. *CUDA C Programming Guide*. NVIDIA Corporation: Santa Clara, CA, USA, 3.2 edition, Oct 2010a.

NVIDIA. *CUDA C Best Practices Guide Version*. NVIDIA Corporation: Santa Clara, CA, USA, 3.2 edition, Aug 2010b. CA Patent 95,050.

M.F. O'Sullivan and E.A.G. Robertson. Critical state parameters from intact samples of two agricultural topsoils. *Soil and Tillage Research*, 39 (3-4):161–173, 1996.

O. Reynolds. On the dilatancy of media composed of rigid particles in contact. *Phil. Mag*, 20(5):46, 1885.

V. Richefeu, F. Radjaı, and M.S. El Youssoufi. Stress transmission in wet granular materials. *The European Physical Journal E: Soft Matter and Biological Physics*, 21(4):359–369, 2006.

K. Sassa, H. Fukuoka, G. Wang, and N. Ishikawa. Undrained dynamic-loading ring-shear apparatus and its application to landslide dynamics. *Landslides*, 1(1):7–19, 2004.

B. Schaffer, M. Stauber, TL Mueller, R. Muller, and R. Schulin. Soil and macro-pores under uniaxial compression. i. mechanical stability of

repacked soil and deformation of different types of macro-pores. *Geoderma*, 146(1-2):183–191, 2008.

D.W. Taylor. Fundamentals of soil mechanics. *Soil Science*, 66(2):161, 1948.

Thrust. http://code.google.com/p/thrust/.

O.R. Walton and R.L. Braun. Viscosity, granular-temperature, and stress calculations for shearing assemblies of inelastic, frictional disks. *Journal of Rheology*, 30(5):949–980, 1986.